Title: Ultra-light, Ultra-stiff Mechanical Metamaterials

Authors: X. Zheng[1*], H. Lee[2], T. H.Weisgraber[1], M. Shusteff[1], J. Deotte[1], E. B. Duoss[1], J. D. Kuntz[1], M. M. Biener[1], Q. Ge[2], J. A. Jackson[1], S. O. Kucheyev[1], N. X. Fang[2*], C. M. Spadaccini[1*]

Affiliations:

[1]Lawrence Livermore National Laboratory, Livermore, CA 94550, USA.

[2]Department of Mechanical Engineering, Massachusetts Institute of Technology, Cambridge, MA 02139, USA.

*Correspondence to: X. Z.: zheng3@llnl.gov, C.M.S.: spadaccini2@llnl.gov, N.X.F.: nicfang@mit.edu

Abstract: The mechanical properties of ordinary materials degrade substantially with reduced density, due to the bending of their structural elements under applied load. We report a class of micro-architected materials that maintain a nearly constant stiffness per unit mass density, even at ultra-low density. This performance derives from a network of nearly isotropic microscale unit cells with high structural connectivity and nanoscale features, whose structural members are designed to carry loads in tension or compression. Production of these microlattices, with constituent materials ranging from polymers to metals and ceramics, is made possible by using projection microstereolithography, an additive micromanufacturing technique, combined with nanoscale coating and post-processing. We found that these materials exhibit ultra-stiff properties across more than three orders of magnitude in density, regardless of the constituent material.

One Sentence Summary:

We report a class of micro-architected materials that change their stiffness linearly with reduced density.

Main Text: Nature has found a way to achieve mechanically efficient materials by evolving cellular structures. Natural cellular materials, including honeycomb (*1*) (wood, cork) and foam-like structures, such as trabecular bone (*2*), plant parenchyma (*3*), and sponge (*4*), combine low weight with superior mechanical properties. For example, lightweight balsa has a stiffness-to-weight ratio comparable to that of steel along the axial loading direction (*5*). Inspired by these naturally occurring cellular structures, manmade lightweight cellular materials fabricated from a wide array of solid constituents are desirable for a broad range of applications including structural components (*6, 7*), energy absorption (*8, 9*), heat exchange (*10, 11*), catalyst supports (*12*), filtration (*13, 14*), and biomaterials (*15, 16*).

However, the degradation in mechanical properties can be drastic as density decreases (*17, 18*). A number of examples among recently reported low-density materials include graphene elastomers (*19*), metallic micro-lattices (*20*), carbon nanotube foams (*21*), and silica aerogels

(*22, 23*). For instance, the Young's modulus of low-density silica aerogels (*22, 23*) decreases to 10 kPa (10^{-5} % of bulk) at a density of less than 10 mg/cm^3 (< 0.5% of bulk).

This loss of mechanical performance is because most natural and engineered cellular solids with random porosity, particularly at relative densities less than 0.1%, exhibit a quadratic or stronger scaling relationship between Young's modulus and density as well as between strength and density. Namely, $E/E_s \sim (\rho/\rho_s)^n$ and $\sigma_y/\sigma_{ys} \sim (\rho/\rho_s)^n$, where E is Young's modulus, ρ is density, σ_y is yield strength, and s denotes the respective bulk value of the solid constituent material property. The power n of the scaling relationship between relative material density and the relative mechanical property depends on the material's microarchitecture. Conventional cellular foam materials with stochastic porosity are known to deform predominantly through bending of their cell walls and struts (*24*). This type of deformation results in relative stiffness scaling with $n = 2$ or 3. A number of approaches in recent years have aimed to reduce this coupling between mechanical properties and mass density (*5, 17, 18, 20, 25-31*). Among these, few fabrication processes are capable of building arbitrary three-dimensional microarchitectures with controlled micro- and nanostructure across a wide range of mass density and material constituents. The desired material properties are thus limited to a narrow density range and specific loading directions.

Improved mechanical properties can arise from a material that contains micro- and nano-scale building blocks arranged in an ordered hierarchy. Among these new designs are metallic microlattices with high recoverability when compressed (*20, 26*), TiN nanotrusses (*32, 33*) and ceramic composite trusses (*34*) that show enhanced fracture toughness of coating materials when the thickness of coating materials is reduced to the nanoscale.

We report a group of ultra-light mechanical metamaterials that maintain a nearly linear scaling between stiffness and density over three orders of magnitude in density, over a variety of constituent materials. We use the term "mechanical metamaterials" to refer to materials with certain mechanical properties defined by their geometry rather than their composition. The materials described here are highly ordered, nearly isotropic, and have high structural connectivity within stretch-dominated, face-centered cubic architectures. The ultra-low density regime is accessed by fabricating microlattices with critical features ranging from ~20 μm down to approximately ~40 nm. The densities of samples produced in this work ranged from 0.87 kg/m^3 to 468 kg/m^3, corresponding to 0.025–20% relative density.

A stretch-dominated unit cell structure, consisting of b struts and j frictionless joints and satisfying Maxwell's criteria, $M = b - 3j + 6 > 0$, is significantly more mechanically efficient, with a higher stiffness-to-weight ratio (defined as E/ρ) than its bend-dominated counterpart. This is attributed to its struts carrying load under compression or tension rather than bending(*17*). A fundamental lattice building block of this type is the octet-truss unit cell (Fig 1 (A)) whose geometric configuration was proposed by Deshpande *et al.*(*35*). The cell has a regular octahedron as its core, surrounded by eight regular tetrahedra distributed on its faces (Fig. S1). All the strut elements have identical aspect ratios, with twelve connected at each node. The cell has a face centered cubic (FCC) structure whose cubic symmetry generates a material with nearly isotropic behavior (*36*). The relative density of such octet-truss unit cells can be approximated by $\rho = 26.64\ (d/L)^2$ (*35*), where L and d are the length and diameter of each beam element. On the macroscale, under uniaxial compressive loading, the relative compressive stiffness and yield strength of these structures theoretically show linear scaling relationships: $E/E_s \sim (\rho/\rho_s)$ and $\sigma/\sigma_s \sim (\rho/\rho_s)$ (*35*). A cubic lattice is readily constructed by periodic packing of the unit cell along its three principal directions (Fig. 1(B) and (C)) (*37, 38*). Alternate orientations of the bulk lattice relative to the unit cell's principal axes can likewise be constructed (Fig. S2), with the fundamental tessellation of space by the unit cell remaining the same. To study how the loading direction and lattice orientation affect their $E\sim\rho$ scaling relationship, octet-truss lattices were analyzed, fabricated, and tested in a variety of orientations ((*39*), Fig S1-Fig S5). In addition to these stretch-dominated lattices, as a point of comparison, a bend-dominated tetrakaidekahedron unit cell (*40, 41*) of the same size scale was generated and the corresponding cubic-symmetric foams (known as Kelvin foams), were fabricated with a variety of densities (Fig. 1(D–F)).

The fabrication of these microlattices is enabled by projection microstereolithography, a layer-by-layer additive micromanufacturing process capable of fabricating arbitrary three-dimensional micro-scale structures (*42, 43*). In contrast to other 3D rapid prototyping methods such as 3D printing and UV projection waveguide systems (*44*), this type of fabrication technology is ideal for 3D lattices with high structural complexity, and with feature sizes ranging from tens of microns to centimeters. By combining projection microstereolithography with nano-scale coating methods, 3D lattices with ultra-low relative densities below 0.1% can be created. The process begins with a photosensitive polymer resin bath; we use either 1, 6-hexanediol diacrylate (HDDA) or poly (ethylene glycol) diacrylate (PEGDA). Shown schematically in Fig. 2(A), the apparatus uses a spatial light modulator—in this case a liquid-crystal-on-silicon chip—as a dynamically reconfigurable digital photomask. A three-dimensional CAD model is first sliced into a series of closely spaced horizontal planes. These two-dimensional image slices are sequentially transmitted to the reflective liquid-crystal-on-silicon chip, which is illuminated with UV light from a light emitting diode array. Each image is projected through a reduction lens onto the surface of the photosensitive resin. The exposed liquid cures, forming a layer in the shape of the two-dimensional image, and the substrate on which it rests is lowered, reflowing a thin film of liquid over the cured layer. The image projection is then repeated with the next image slice forming the subsequent layer. Our polymer microlattices were fabricated in tens of minutes and have features spanning size scales from 10 to 500 μm. For mechanical testing purposes, all materials described here were fabricated as blocks of various sizes consisting of multiple unit cells (Table S1). Fig. 2(B) and (F) show scanning electron micrographs (SEM) of the as-built polymer lattice and unit cell.

Although projection microstereolithography requires a photopolymer, other constituent materials, such as metals and ceramics, can be incorporated with additional processing. Using the base polymer lattice as a template, we are able to convert the structures to metallic and ceramic microlattices. Metallic lattices were generated via electroless nickel plating on the as-formed HDDA. The thickness of the metal coating is controlled by the plating time, yielding metal films from 100 nm to 2 μm. The polymer template is subsequently removed by thermal decomposition, leaving behind the hollow-tube nickel-phosphorus (Ni-P) stretch-dominated microlattice shown in Fig. 2(C) and (G).

A similar templating approach is used to generate hollow-tube aluminum oxide (amorphous Al_2O_3, alumina) microlattices; however, the coating is produced by atomic layer deposition (ALD), a gas phase process, rather than liquid phase processing. The resulting hollow-tube microlattices have alumina thicknesses from ~40 to 210 nm, with an example shown in Fig. 2(D) and (H), with corresponding material weight density ranging from less than 1 kg/m^3 to 10.2 kg/m^3.

Loading the resin bath with nanoparticles can further expand the base material set. Solid Al_2O_3 ceramic lattices were prepared in the microlithography system by using photosensitive PEGDA liquid prepolymer loaded with ~150 nm alumina nanoparticles (Baikowski Inc, approximately 12.5% alumina by volume). The same sequential lithographic exposure process produced a microlattice made of a hybrid of solid PEGDA and alumina nanoparticles. These hybrid lattices are converted to pure Al_2O_3 octet-truss microlattices through a sintering procedure (*39*). An example of this structure is shown in Fig. 2(E) and (I). The parameters and properties for a selection of our stretch-dominated mechanical metamaterials and bend-dominated foams are summarized in Table S1. The densities of all samples were calculated by measuring the weight and fabricated dimensions of the completed microlattices.

The microstructured mechanical metamaterials were tested to determine their Young's modulus E and uniaxial compressive strength σ_y, defined as the crushing stress of the material. Uniaxial compression studies of all microlattices with the same cubic dimensions were conducted on an MTS Nano Indenter XP, equipped with a flat punch stainless steel tip with a diameter of 1.52 mm. During 20 consecutive compression cycles up to 10% strain, we observed typical viscoelastic behavior for the polymer microlattices with pronounced hysteresis with loading rate dependent Young's modulus. The Young's moduli for all polymer microlattices and foams were extracted at loading rate at 87.2 nN/s, corresponding to a strain rate of 10^{-3} s^{-1}. Uniaxial compression of these structures is shown in Movies S1-S3. Representative stress-strain curves from uniaxial compression crushing tests for determining the compressive strength of octet-truss microlattices made of solid HDDA polymer, hollow-tube Ni-P metal, and solid alumina are shown in Fig. S7 (A), (B) and Fig. S8 (A) respectively. Bulk HDDA polymer, cured by UV crosslinking a solid sample of similar dimensions to the octet-truss lattices, was determined to have Young's modulus and yield stress values of E_s = 530 MPa and σ_{ys}= 86 MPa, respectively. The bulk property values for other constituent materials and the detailed methods of measurement are given in supplementary sections (*39*).

The results of these mechanical tests, together with the bend-dominated tetrakaidekahedron-based Kelvin foams fabricated from the base HDDA polymer, are summarized in Fig. 3(A) and Fig. 3(B), which plot the relative Young's modulus and strength against the relative mass density, respectively. Fig. 4 shows the location of these material properties on the stiffness versus density material selection chart, together with other recently reported ultra-light materials for comparison. The stretch-dominated microlattices populate the highly desirable ultra-light, ultra-stiff space toward the upper left of the chart (*17*) and have stiffness-to-weight ratios that do not substantially degrade as density decreases by several orders of magnitude. In contrast to the common bend-dominated $E/E_s \sim (\rho/\rho_s)^2$ scaling of open-cell stochastic foams such as silica aerogels and carbon foams, our stretch-dominated microlattice materials demonstrate the desired linear relationship of $E/E_s \sim \rho/\rho_s$, approaching the theoretical limit, and exhibit this remarkable scaling relationship over three orders of magnitude in density and across all constituent materials studied. These octet-truss lattice materials are highly isotropic, so the scaling of stiffness with density does not vary with the orientation of the lattice (Fig S4), as confirmed by our studies of different loading directions. These lattices have the highest specific stiffness when the lattice is loaded normal to the (111) plane, which is closest-packed within the FCC architecture.

In the ultralow-density regime (relative density < 0.1%), we observed markedly different compression behavior in hollow-tube ALD ceramic octet-truss microlattices, compared to solid ceramic lattices at higher relative densities (8–20%). The hollow-tube ceramic microlattices with nanoscale wall thicknesses showed smoother behavior with progressively fewer discontinuities in their stress-strain curves (Fig. S8 (A) and (B)) in contrast to solid microstrut ceramic lattices with catastrophic, fracture-dominated behavior. The loading-unloading curves of hollow-tube

Al_2O_3 lattices revealed elastic behavior followed by a nonlinear response on each loading cycle. Although relative compressive stiffness and relative density initially follow a nearly linear scaling law, the transition from conventional brittle behavior (in low-density ceramic materials) to more "ductile" mechanical behavior (in ultra-light materials with nanoscale wall thicknesses) suggests a transition from a fracture-dominated failure mode to a buckling-dominated failure mode with suppression of the catastrophic failure seen in solid Al_2O_3 octet-truss lattices. These differences in compressive behavior between solid and hollow-tube ceramic octet-truss lattices are primarily attributed to local buckling induced by the high aspect ratio of the strut length to nanoscale wall thickness, in contrast to nanoscale TiN trusses (*32*) and ceramic composite (*34*) where the aspect ratio is low enough to allow the nanoscale strengthening effect of the wall thickness to dominate. For example, the ratio of strut length to nanoscale wall thickness in Fig. S8(B) is approximately 1400:1 and contributes to its large compression strain, governed by $\varepsilon \sim (1/\rho)^{0.5}$ (*17*). Thus, the relative compressive strength transitions from the nearly linear scaling law governing the stretch-dominated failure mode at an approximate density near 0.08% to a scaling power of 2.7, as indicated in Fig. 3(B). In the same figure, a similar transition from yielding dominated to buckling dominated failure at an approximate relative density of 0.2% is evident in Ni-P lattices, consistent with the trend observed on bend-dominated metallic microlattices (*26*).

When an ultralow-density metallic microlattice is bend-dominated, its stiffness degrades significantly with reduced density. An example of this is the Ni-P lattice reported by Schaedler et al. (*20*), whose specific stiffness (stiffness to weight ratio) degrades from 0.23×10^6 m^2/s^2 to 0.05×10^6 m^2/s^2 as density is reduced from 40 mg/cm^3 to 14 mg/cm^3 (*45*). Significantly, our Ni-P stretch-dominated metallic lattice is not only much stiffer in the same density range, its specific stiffness stays nearly constant, measured as 1.8×10^6 m^2/s^2 and 2.1×10^6 m^2/s^2 at densities of 14 mg/cm^3 and 40 mg/cm^3, respectively. Similarly, in a recent report of high-strength microarchitected ceramic composites (*34*), their strength performance approaches the linear scaling relationship over a narrow density range, and only when loaded in a direction optimized for their anisotropic architecture. Our metamaterials, in contrast, maintain their mechanical efficiency over a broad density regime, without substantial degradation in specific stiffness, owing to the nearly linear $E \sim \rho$ scaling relationship.

We have shown that these high mechanical efficiencies are possible across a range of constituent materials. Fabricating ordered lattice structures at these length scales brings them into the regime in which it becomes possible to interact with the structure as a material.

References and Notes:

1. K. Ando, H. Onda, Mechanism for deformation of wood as a honeycomb structure I: Effect of anatomy on the initial deformation process during radial compression. *J Wood Sci* **45**, 120 (1999).
2. T. M. Ryan, C. N. Shaw, Trabecular bone microstructure scales allometrically in the primate humerus and femur. *P Roy Soc B-Biol Sci* **280**, (May 7, 2013).
3. P. Van Liedekerke *et al.*, A particle-based model to simulate the micromechanics of single-plant parenchyma cells and aggregates. *Phys Biol* **7**, (Jun, 2010).
4. J. H. Shen, Y. M. Xie, X. D. Huang, S. W. Zhou, D. Ruan, Compressive Behavior of Luffa Sponge Material at High Strain Rate. *Advances in Engineering Plasticity Xi* **535-536**, 465 (2013).
5. J. A. Kepler, Simple stiffness tailoring of balsa sandwich core material. *Compos Sci Technol* **71**, 46 (2011).

6. L. Valdevit, A. J. Jacobsen, J. R. Greer, W. B. Carter, Protocols for the Optimal Design of Multi-Functional Cellular Structures: From Hypersonics to Micro-Architected Materials. *J Am Ceram Soc* **94**, 1 (Jun, 2011).
7. N. Lyu, B. Lee, K. Saitou, Optimal subassembly partitioning of space frame structures for in-process dimensional adjustability and stiffness. *J Mech Design* **128**, 527 (May, 2006).
8. T. A. Schaedler *et al.*, Designing Metallic Microlattices for Energy Absorber Applications. *Adv Eng Mater* **16**, 276 (2014).
9. K. J. Maloney *et al.*, Microlattices as architected thin films: Analysis of mechanical properties and high strain elastic recovery. *APL Materials* **1**, (2013).
10. L. Valdevit, A. Pantano, H. A. Stone, A. G. Evans, Optimal active cooling performance of metallic sandwich panels with prismatic cores. *Int J Heat Mass Tran* **49**, 3819 (Oct, 2006).
11. M. Q. Li, X. Shi, Microstructure and thermal conductivity of flexible and micro-porous calcium silicate insulation material. *Rare Metal Mat Eng* **36**, 575 (Aug, 2007).
12. O. Y. Kwon, H. J. Ryu, S. Y. Jeong, Porous layered carbon as catalyst support material for PEMFC. *J Ind Eng Chem* **12**, 306 (Mar, 2006).
13. R. A. Olson, L. C. B. Martins, Cellular ceramics in metal filtration. *Adv Eng Mater* **7**, 187 (Apr, 2005).
14. P. Day, H. Kind, Filtration of Irons with Cellular Ceramic Filters. *Mod Cast* **74**, 16 (1984).
15. S. Baudis *et al.*, Elastomeric degradable biomaterials by photopolymerization-based CAD-CAM for vascular tissue engineering. *Biomed Mater* **6**, (Oct, 2011).
16. K. Arcaute, B. K. Mann, R. B. Wicker, Fabrication of Off-the-Shelf Multilumen Poly(Ethylene Glycol) Nerve Guidance Conduits Using Stereolithography. *Tissue Eng Part C-Me* **17**, 27 (Jan, 2011).
17. J. L. Gibson, F. M. Ashby, *Cellular Solids: Structure and Properties*. Book (Cambridge University Press, Cambridge, UK, 2001).
18. H. Y. Fan *et al.*, Modulus-density scaling behaviour and framework architecture of nanoporous self-assembled silicas. *Nat Mater* **6**, 418 (Jun, 2007).
19. L. Qiu, J. Z. Liu, S. L. Y. Chang, Y. Z. Wu, D. Li, Biomimetic superelastic graphene-based cellular monoliths. *Nat Commun* **3**, (Dec, 2012).
20. T. A. Schaedler *et al.*, Ultralight Metallic Microlattices. *Science* **334**, 962 (Nov 18, 2011).
21. M. A. Worsley, S. O. Kucheyev, J. H. Satcher, A. V. Hamza, T. F. Baumann, Mechanically robust and electrically conductive carbon nanotube foams. *Appl Phys Lett* **94**, (Feb 16, 2009).
22. T. M. Tillotson, L. W. Hrubesh, Transparent Ultralow-Density Silica Aerogels Prepared by a 2-Step Sol-Gel Process. *J Non-Cryst Solids* **145**, 44 (Aug, 1992).
23. S. O. Kucheyev *et al.*, Super-Compressibility of Ultralow-Density Nanoporous Silica. *Adv Mater* **24**, 776 (Feb 7, 2012).
24. L. J. Gibson, Cellular solids. *Mrs Bull* **28**, 270 (Apr, 2003).
25. K. Tantikom, Y. Suwa, T. Aizawa, In-plane compression response of regularly cell-structured materials. *Mater Trans* **45**, 509 (Feb, 2004).
26. A. Torrents, T. A. Schaedler, A. J. Jacobsen, W. B. Carter, L. Valdevit, Characterization of nickel-based microlattice materials with structural hierarchy from the nanometer to the millimeter scale. *Acta Mater* **60**, 3511 (2012).
27. C. Q. Dam, R. Brezny, D. J. Green, Compressive Behavior and Deformation-Mode Map of an Open Cell Alumina. *J Mater Res* **5**, 163 (Jan, 1990).
28. J. K. Cochran, K. J. Lee, D. McDowell, T. Sanders, Multifunctional metallic honeycombs by thermal chemical processing. *Processsing and Properties of Lightweight Cellular Metals and Structures*, 127 (2002).
29. J. Zhang, M. F. Ashby, The out-of-plane properties of honeycombs. *Int J Mech Sci* **34**, 475 (1992).
30. D. Rayneau-Kirkhope, Y. Mao, R. Farr, Ultralight Fractal Structures from Hollow Tubes. *Phys Rev Lett* **109**, (Nov 16, 2012).
31. K. C. Cheung, N. Gershenfeld, Reversibly Assembled Cellular Composite Materials. *Science* **341**, 1219 (September 13, 2013, 2013).
32. D. Jang, L. R. Meza, F. Greer, J. R. Greer, Fabrication and deformation of three-dimensional hollow ceramic nanostructures. *Nat Mater* **12**, 893 (2013).
33. L. Meza, J. Greer, Mechanical characterization of hollow ceramic nanolattices. *J Mater Sci* **49**, 2496 (2014/03/01, 2014).
34. J. Bauer, S. Hengsbach, I. Tesari, R. Schwaiger, O. Kraft, High-strength cellular ceramic composites with 3D microarchitecture. *Proceedings of the National Academy of Sciences*, (February 3, 2014, 2014).

35. V. S. Deshpande, N. A. Fleck, M. F. Ashby, Effective properties of the octet-truss lattice material. *J Mech Phys Solids* **49**, 1747 (Aug, 2001).
36. J. D. Renton, *Elastic Beams and Frames*. (Horwood Publishing Limited Chichester, ed. 2, 2002).
37. S. Hyun, J. E. Choi, K. J. Kang, Effects of imperfections on the mechanical behavior of a wire-woven bulk Kagome cellular metal under compression. *Comp Mater Sci* **46**, 73 (Jul, 2009).
38. H. L. Fan, F. N. Jin, D. N. Fang, Nonlinear mechanical properties of lattice truss materials. *Mater Design* **30**, 511 (Mar, 2009).
39. Materials and methods are available as supplementary material on Science Online. .
40. W. Y. Jang, S. Kyriakides, A. M. Kraynik, On the compressive strength of open-cell metal foams with Kelvin and random cell structures. *Int J Solids Struct* **47**, 2872 (Oct 15, 2010).
41. Y. Takahashi, D. Okumura, N. Ohno, Yield and buckling behavior of Kelvin open-cell foams subjected to uniaxial compression. *Int J Mech Sci* **52**, 377 (Feb, 2010).
42. X. Y. Zheng *et al.*, Design and optimization of a light-emitting diode projection micro-stereolithography three-dimensional manufacturing system. *Rev Sci Instrum* **83**, (Dec, 2012).
43. C. Sun, N. Fang, D. M. Wu, X. Zhang, Projection micro-stereolithography using digital micro-mirror dynamic mask. *Sensor Actuat a-Phys* **121**, 113 (May 31, 2005).
44. A. J. Jacobsen, W. Barvosa-Carter, S. Nutt, Micro-scale Truss Structures formed from Self-Propagating Photopolymer Waveguides. *Adv Mater* **19**, 3892 (2007).
45. L. M. Moreau *et al.*, Unintended phosphorus doping of nickel nanoparticles during synthesis with TOP: a discovery through structural analysis. *Nano Lett* **12**, 4530 (Sep 12, 2012).
46. V. S. Deshpande, M. F. Ashby, N. A. Fleck, Foam topology: bending versus stretching dominated architectures. *Acta Mater* **49**, 1035 (2001).
47. M. A. Puso, "NIKE3D: A Nonlinear, Implicit, Three-Dimensional Finite Element Code for Solid and Structural Mechanics" (Lawrence Livermore National Laboratory Livermore, California, USA, 2012).
48. D. Ruffoni, J. William Chapman Dunlop, P. Fratzl, R. Weinkamer, Effect of minimal defects in periodic cellular solids. *Philos Mag* **90**, 1807 (2010/05/07, 2010).
49. D. D. Symons, N. A. Fleck, The Imperfection Sensitivity of Isotropic Two-Dimensional Elastic Lattices. *J Appl Mech* **75**, 051011 (2008).
50. M. Alkhader, M. Vural, Mechanical response of cellular solids: Role of cellular topology and microstructural irregularity. *Int J Eng Sci* **46**, 1035 (2008).
51. N. E. R. Romijn, N. A. Fleck, The fracture toughness of planar lattices: Imperfection sensitivity. *J Mech Phys Solids* **55**, 2538 (2007).
52. H. Li, J. J. Vlassak, Determining the elastic modulus and hardness of an ultra-thin film on a substrate using nanoindentation. *J Mater Res* **24**, 1114 (Mar, 2009).
53. W. C. Oliver, G. M. Pharr, An improved technique for determining hardness and elastic modulus using load and displacement sensing indentation experiments. *J Mater Res* **7**, 1564 (1992).
54. S. Y. Chang, Y. S. Lee, H. L. Hsiao, T. K. Chang, Mechanical properties and deformation behavior of amorphous nickel-phosphorous films measured by nanoindentation test. *Metall Mater Trans A* **37A**, 2939 (Oct, 2006).
55. R. Weil, K. Parker, in *Electroless Plating: Fundamentals and Applications,* J. B. H. O. Mallory, Ed. (William Andrew/Noyes, Norwich, NY, 1990).

Acknowledgments: This work performed under the auspices of the U.S. Department of Energy by Lawrence Livermore National Laboratory under Contract DE-AC52-07NA27344. Funding support from LDRD Strategic Initiative 11-SI-005 and DARPA MCMA (Materials with Controlled Microstructural Architecture, Program Manager Dr. Judah Goldwasser) is gratefully acknowledged. The authors at Lawrence Livermore National Laboratory wish to acknowledge Howard Rathbun for useful discussions on modeling the lattice structures as well as Dr. Marcus Worsley for taking SEM images and Christopher Harvey for his technical support (LLNL-JRNL-640334).

Fig. 1. Architecture of stretch-dominated and bend-dominated unit cells and lattices. (A) Mechanical response to compressive loading of a stretch-dominated octet-truss unit cell. (B)

Octet-truss unit cells packed into a cubic microlattice. (C) SEM image of a stretch-dominated lattice material that is composed of a network of octet-truss unit cells. (D) Mechanical response to compressive loading of a bend-dominated tetrakaidekahedron unit cell. (E) Tetrakaidekahedron unit cell packed into a cubic bend-dominated lattice (Kelvin foam). (F) SEM image of a bend-dominated lattice that is composed of a network of tetrakaidekahedron unit cells.

Fig. 2. Fabrication of ultra-light, ultra-high stiffness stretch-dominated microlattices. (A) Projection microstereolithography, a layer-by-layer technique capable of fabricating arbitrary, microscale, three-dimensional structures with ~5 μm resolution; the SEM imageon the right is the fabricated octet-truss unit cell. (B)–(E) Octet-truss microlattices with varied constituent materials and configurations: (B) solid polymer HDDA. (C) hollow-tube metallic Ni-P, (D) hollow-tube ceramic (alumina) (E) solid ceramic (alumina). (F)-(I) are magnified views of the struts of the microlattices in (B)-(E), respectively.

Fig. 3. (A) Relative stiffness as a function of relative density for stretch-dominated microlattices and bend-dominated microlattices. Stretch-dominated materials exhibit a linear stiffness–density relationship of $E \sim \rho$, whereas bend-dominated materials soften as $E \sim \rho^2$ or worse, as shown by their slopes in the plot. (B) Relative strength as a function of relative density for stretch-dominated and bend-dominated microlattices.

Fig. 4. An Ashby chart plotting the compressive stiffness vs. the density of ultra-light, ultra-stiff mechanical metamaterials compared to other previously reported materials. Dotted lines indicate contours of constant stiffness–density ratio $c = E/\rho$ (m^2/s^2).

Supplementary Materials:

Materials and Methods

Figures S1-S9

Table S1

Movies S1-S3

References (*46-55*)

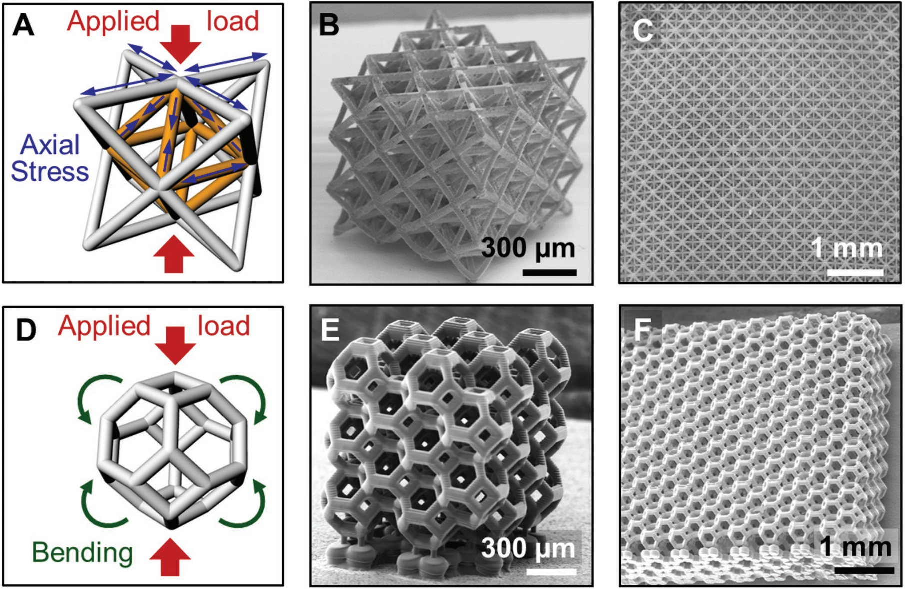
A
Applied load
Axial Stress
B
300 µm
C
1 mm
D
Applied load
Bending
E
300 µm
F
1 mm

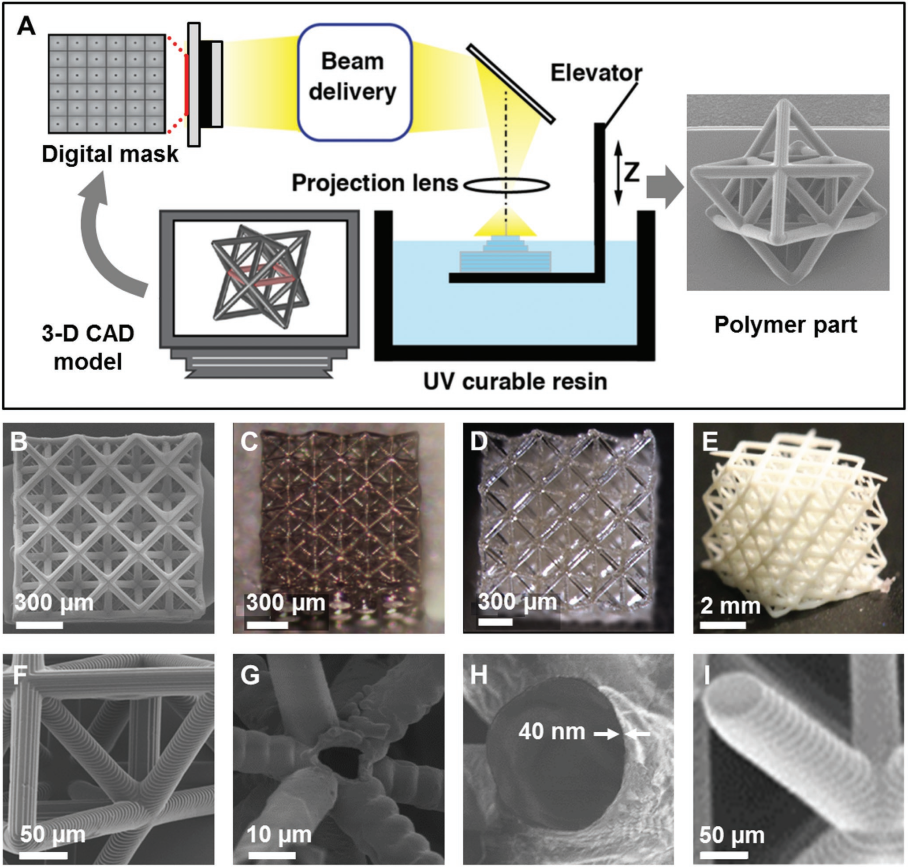
A
Digital mask
Beam delivery
Elevator
Projection lens
Z
3-D CAD model
UV curable resin
Polymer part
B
300 µm
C
300 µm
D
300 µm
E
2 mm
F
50 µm
G
10 µm
H
40 nm
I
50 µm

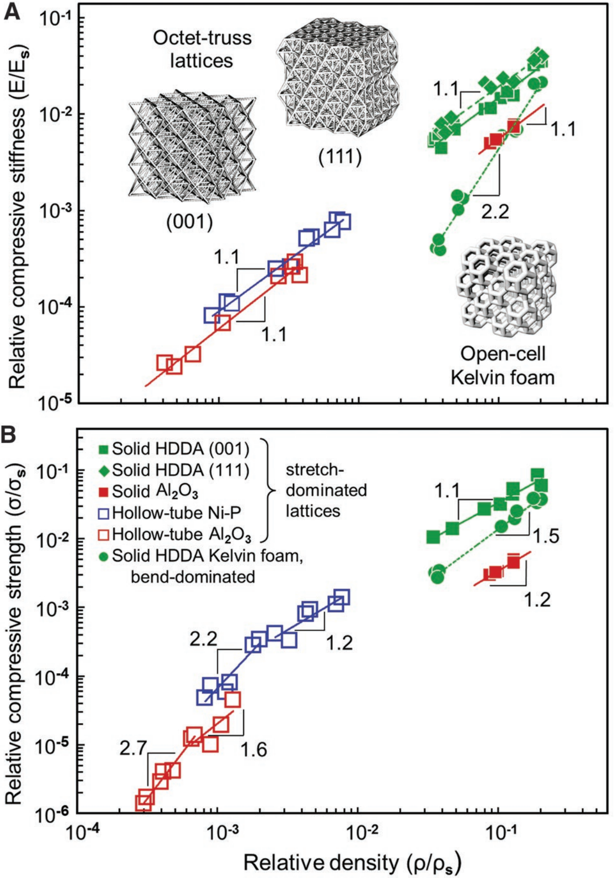
A
Relative compressive stiffness (E/E$_s$)
10^{-1}
10^{-2}
10^{-3}
10^{-4}
10^{-5}
Octet-truss lattices
(001)
(111)
1.1
1.1
2.2
1.1
1.1
Open-cell Kelvin foam
B
Relative compressive strength (σ/σ$_s$)
10^{-1}
10^{-2}
10^{-3}
10^{-4}
10^{-5}
10^{-6}
■ Solid HDDA (001)
◆ Solid HDDA (111)
■ Solid Al$_2$O$_3$
□ Hollow-tube Ni-P
□ Hollow-tube Al$_2$O$_3$
stretch-dominated lattices
● Solid HDDA Kelvin foam, bend-dominated
1.1
1.5
1.2
2.2
1.2
2.7
1.6
10^{-4}
10^{-3}
10^{-2}
10^{-1}
Relative density (ρ/ρ$_s$)

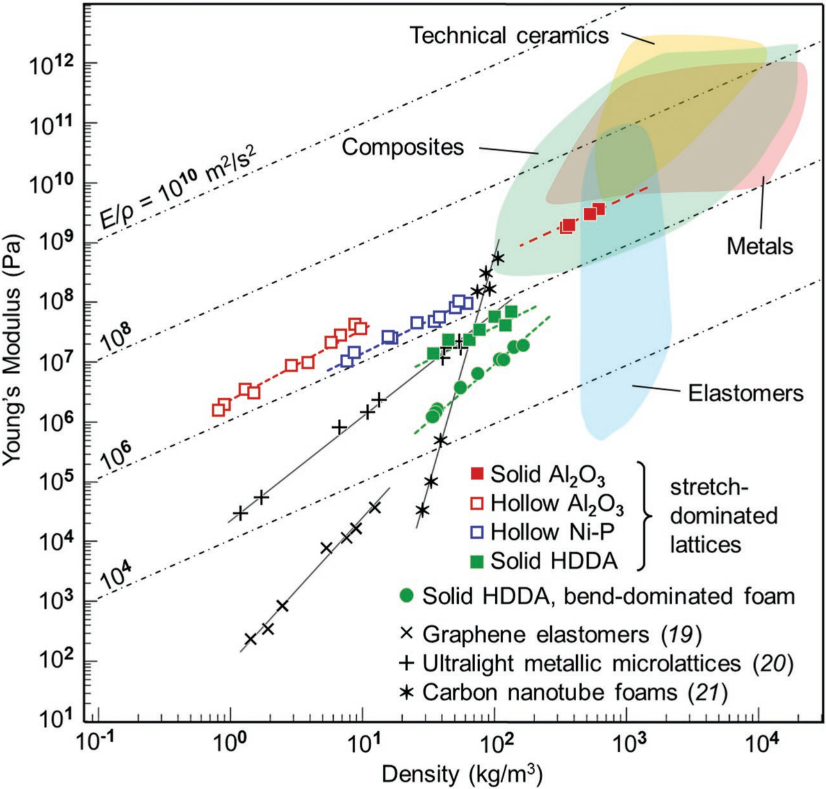
Technical ceramics
Composites
Metals
Elastomers
$E/\rho = 10^{10}$ m^2/s^2
10^8
10^6
10^4
Young's Modulus (Pa)
10^{12}
10^{11}
10^{10}
10^9
10^8
10^7
10^6
10^5
10^4
10^3
10^2
10^1
10^{-1}
10^0
10^1
10^2
10^3
10^4
Density (kg/m^3)
■ Solid Al_2O_3
□ Hollow Al_2O_3
□ Hollow Ni-P
■ Solid HDDA
stretch-dominated lattices
● Solid HDDA, bend-dominated foam
× Graphene elastomers (*19*)
+ Ultralight metallic microlattices (*20*)
✶ Carbon nanotube foams (*21*)

Supplementary Materials for

Ultra-light, Ultra-stiff Mechanical Metamaterials

Xiaoyu Zheng[1*], Howon Lee[2], Todd H Weisgraber[1], Maxim Shusteff[1], Joshua R. Deotte[1], Eric Duoss[1], Joshua D. Kuntz[1], Monika M. Biener[1], Qi Ge[2], Julie A. Jackson[1], Sergei O. Kucheyev[1], Nicholas X. Fang[2*], Christopher M. Spadaccini[1*]

Correspondence to: Christopher M. Spadaccini (spadaccini2@llnl.gov),
Nicholas X. Fang (nicfang@mit.edu)
Xiaoyu Zheng (zheng3@llnl.gov)

This PDF file includes:

Materials and Methods
Figs. S1 to S9
Table S1
Captions for Movies S1 to S3

Other Supplementary Materials for this manuscript includes the following:

Movies S1 to S3

Materials and Methods

S1. Octet-truss lattice geometric configurations

The octet-truss lattice structures in this study satisfy the Maxwell deterministic stability criteria for a stretch-dominated pin-jointed frame (*17, 46*). As described in the main article, the face-centered cubic (FCC) unit cell has a regular octahedron core with regular tetrahedra affixed to each face, such that twelve strut elements connect at each node. The unit cell's cubic symmetry (detailed in Figure S1) results in a material with nearly isotropic properties (*36*). The microstructured lattice material is produced by "stacking" unit cells with each strut shared between two neighboring cells – i.e. periodically repeating unit cell elements along three orthogonal axes. We refer to different lattice orientations by the Miller indices of the lattice plane that forms a flat face to which loading is applied. Thus, a (111)-oriented lattice has a (111) plane at its top surface, to which uniaxial compressive loading is applied in the [111] direction.

We carried out finite-element (FEM) studies of four different lattice orientations: (001), (111), $(11\bar{2})$, and $(1\bar{1}0)$ shown in Fig.S2. These studies complemented and expanded upon the experimental measurements of (001)- and (111)-oriented solid polymer HDDA lattices, fabricated by projection micro-stereolithography. The finite element simulations were performed with the NIKE3D fully implicit solver, developed at Lawrence Livermore National Laboratory (*47*). Each strut in the octet-truss lattice was represented by a single Hughes-Liu beam element (Fig S3). The simulations for the [001] loading direction contained 27 repeating unit cells and 172 nodes. For the other loading directions, the FEM model was based on the geometry of the stereolithography-fabricated part for the (111) orientation (Figure S2 compare (B), (C) and (D)) and contained 265 nodes. Using a linear elastic materials model based on the properties of HDDA, the relative stiffness at each density was derived from the slope of the stress response with applied loading. To mimic the experimental conditions, for each loading direction, boundary conditions were established for two sets of nodes contained within defined upper and lower planar surfaces with normals coincident with the load (arrows in Fig. S3). A linear displacement was applied to the nodes of the upper plane, while the lower plane nodes remained fixed. The remaining nodes were unconstrained.

It is clear from the FEM results in Fig. S4 that the overall linear scaling relationship does not change as the major orientation changes. This confirms that the overall stretch-dominated behavior operates regardless of loading direction. However, the linear proportionality constant degrades as the direction deviates from (111) plane which offers the highest stiffness-to-weight ratio. These scaling stiffness constants in different orientation planes, namely, $\frac{E}{E_S} = C_{(hkl)} \frac{\rho}{\rho_S}$ are found to be $C_{(001)} = 0.2412$, $C_{(111)} = 0.3884$, $C_{(1\bar{1}0)} = 0.2269$, and $C_{(11\bar{2})} = 0.1596$.

These findings are supported by mechanical testing of real structures in a subset of these orientations (Fig. S5(A)). The results of uniaxial compression tests on the solid polymer HDDA lattices with (001) and (111) orientations, carried out as detailed in the main article, are summarized in Fig. S5(B), and compared with the directional sensitivity of honeycomb structures and bend-dominated open-cell foam structures. It is apparent that the honeycomb, when loaded out of plane – i.e. perpendicular to the axis of the hexagonal prisms (*29*) has the optimal linear scaling between *E* and *r*, whereas when loaded in-plane, its stiffness suffers greatly (*25, 29*). This was confirmed in a recent study of composite polymer-ceramic microarchitectures, where only a honeycomb optimized for out-of-plane loading exhibited the ideal linear stiffness-density scaling relationship (*34*). In contrast, the octet-truss material, due to its symmetry, exhibits optimal linear scaling of E with r for all of the orientations studied here, with the (111) orientation slightly stiffer than the (001) orientation.

S2. Octet-truss lattice defect sensitivity

Defects in the lattice material building blocks may have crucial effects on the macroscopic properties of the material, and there are numerous prior studies of other cellular materials. For honeycomb structures, for example, Ruffoni et al. thoroughly investigated the relationship between geometric defects and their macroscopic properties, and calculated the strain energy density around a single defect within two-dimensional cellular solids (*48*). This has important implications for the honeycomb, which is one of the most widely used cellular structures, and sheds light on other 2D and 3D cellular structures. Symons and Fleck (*49*) present a detailed treatment of the role of various microstructural imperfections (missing struts, misplaced joints, and deformed cell walls) upon the in-plane effective properties of three isotropic lattices: hexagonal, triangular and Kagome. Alkhader and Vural compare the influence of defects in honeycomb structures, with tetragonal and triangular lattices (*50*). The weakening of mechanical properties due to misplaced joints is numerically explored in a parallel study by Romijn and Fleck for three isotropic lattices, as well as two orthotropic topologies: square and diamond-celled (*51*). All these studies conclude that the defect sensitivity of modulus and fracture toughness for each lattice is highly dependent on its nodal connectivity, consistent with the arguments of Deshpande et al (*46*). Lattices with a high connectivity value of 6 or more, such as the triangular lattice, are highly insensitive to defects, compared to square lattices. The misplaced joints have a negligible effect upon their mechanical properties.

This analysis is highly favorable for the octet-truss lattice, with its exceptionally high nodal connectivity of 12. In contrast, some lattices, such as the Kagome, have a connectivity value that is in a transitional range. The response of these lattices can be bending- or stretching-dominated, depending on the degree of imperfection. For instance, under uniform loading a square lattice deforms by strut stretching, but upon the introduction of a defect such as a macroscopic crack the struts deform by a combination of stretching and bending. Thus, the moduli and strength of this type of topology are highly sensitive to imperfections.

For generality, we chose to study the defect sensitivity of the octet-truss lattices using an FEM approach. While it is possible to generate parts with controlled defects, this would significantly limit the number and type of defects within the study. Moreover, misplaced joints and node positions are the most common defects in 3D manufactured trusses. Here, we model defects that are displacements of the node positions from their proper locations within the octet-truss geometry. We compare a perfect octet-truss lattice with lattices containing joint mismatches and irregularities in the shape of the trusses, which arise from the displaced node positions. In order to simulate geometric imperfections from a more generic perspective, rather than single nodal defects, the positions of all nodes were translated in all three directions by a distance described by a Gaussian distribution with zero mean and a standard deviation of δ=5-20% of the strut length. Then, as in the study of different orientations described above, a linear displacement was applied to the upper plane nodes, while the lower plane nodes remained fixed, and all other nodes were unconstrained. For each perturbation amplitude, the sample size was 100 simulations. Fig S6(A) shows models constructed in NIKE 3D with prescribed defect levels from 0 to 20% of the strut length. Fig S 6 (B) shows the effect of geometric imperfections on the relative stiffness of the octet-truss lattice in the (001) orientation, with each cluster of points at a specific relative density spanning the range of defect levels. The sensitivity to defects can be assessed by examining the slope of the stiffness as a function of defect level (Fig S6(C)). It is evident from these results that the octet-truss lattice is highly insensitive to geometric imperfections, thanks to its high nodal connectivity. Figures S6 (B) and (D) confirm that the octet-truss lattice remains stretch-dominated, with only a slight reduction in its proportional stiffness constant, even when perturbed at a defect level of 20%. We find no evidence that any bending mechanism can be activated by introducing defects.

S3. Fabrication of hollow-tube Ni-P microlattices and measurement of bulk properties

All chemicals for electroless nickel deposition were obtained from Sigma-Aldrich (Milwaukee, WI) unless otherwise indicated. To prepare each sample for electroless nickel deposition, the sample was first cleaned by immersing in an acetone bath with gentle agitation for 2 minutes. After rinsing in deionized (DI) water for 30 seconds, the sample was immersed in a 1 M NaOH solution for 2 minutes followed by rinsing in DI water for 1 minute. Next, the sample surface was sensitized by immersing in an aqueous solution containing 3.5 g/L of $SnCl_2 \cdot 2H_2O$ and 5.0 mL/L 37% HCl for 2 minutes followed by rinsing in DI water for 30 seconds. After sensitization, the sample surface was activated with palladium catalyst by immersing in an aqueous solution containing 0.5 g/L PdCl and 4.0 mL/L 37% HCl for 2 minutes followed by rinsing in DI water for 30 seconds. After activation, the surface was metallized with nickel by immersing in a bath consisting of equal parts by volume of EdgeMet Electroless Nickel Kit A and B (Buehler, Lake Bluff, IL). This step was performed at 80°C with vigorous stirring. The coating thickness was controlled by varying the time of the metallization step between 1–20 minutes. Following this step, the sample was removed and rinsed with DI water for 30 seconds and allowed to air dry. Subsequently, the polymer interior was removed via thermal decomposition by heat-treating in a box furnace in air at 500°C for 4 hours. This last step yielded hollow-tube nickel-phosphorus microlattices.

The mechanical properties for the base electroless plated Ni-P material were measured via nanoindentation with a Berkovich diamond tip. Indents were carried out on a Ni-P film approximately 2 μm thick, deposited on a silicon substrate by the same method described above. The film was subsequently annealed at 500 °C for 4 hours, to mimic the conditions experienced during preparation of hollow-tube Ni-P microlattices. Averaged values were collected from a least n=6 different indents on each sample, made at a constant loading strain rate of 0.05 s^{-1}. To avoid substrate compliance effects, indenter penetration depth was limited to no more than 10% of the total film thickness. Stiffness (Young's modulus) and hardness were calculated based on continuous stiffness measurement (CSM) (*52*) according to the Oliver-Pharr method (*53*). The measured Young's modulus value of 97 GPa after annealing is toward the low end, but well within the range of reported values for Ni-P (*54, 55*). The measured hardness value H=5.2 GPa was used to calculate the yield strength of Ni-P as $\sigma_s \approx H/3 = 1.73$GPa.

S4. Fabrication of AL_2O_3 hollow-tube microlattices and measurement of bulk properties

Nanoscale Al_2O_3 films were deposited by ALD using the well-established trimethyl-aluminum ($AlMe_3$/ H_2O) process in a warm wall reactor (wall and stage temperature of 125ºC). Long pulse, pump, and purge times (90 seconds each) were used to ensure uniform coatings throughout the porous material. The film thickness was controlled by adjusting the number of

ALD cycles, and the growth rate per cycle was calculated from the measured mass gain, the known surface area of lattice structures, and density of ALD Al_2O_3. This rate was found to be ~0.25 nm per cycle. The bimaterial hybrid polymer-Al_2O_3 microlattices were then heat-treated in a box furnace in air at 500°C for 4 hours to remove the polymer template, leaving behind the Al_2O_3 hollow-tube octet-truss lattices.

For characterization of the ALD material Al_2O_3 hollow-tube octet truss lattices, approximately 200 nm of Al_2O_3 was deposited onto a silicon substrate at 125 ºC following the procedure above. ALD Al_2O_3 film properties were characterized via nanoindentation similarly to the methods used for Ni-P described in S3. The values of Young's modulus and yield strength measured for ALD alumina are $E_s = 153$ GPa and $\sigma_s = 2.2$ GPa, respectively, with a calculated mass density of 2900 kg/m^3.

S5. Fabrication of solid AL_2O_3 ceramic microlattices

Ceramic loaded polymer lattices were initially created with 150 nm Al_2O_3 nanoparticles (Baikowski, Inc.) loaded at approximately 12.5% alumina by volume in the PEGDA prepolymer. The ceramic-loaded polymer lattice was fabricated through projection microstereolithography using the same procedure as described in the main text. Subsequently a sintering process was used to remove the polymer and densify the alumina. This began with staged calcination in air (120ºC for water removal, 220ºC for volatile hydrocarbon, 420ºC for combustion of hydrocarbon, and 600ºC for burning out residual carbon) and a final dwell at 1000ºC for 2 hours. Then, the sintering process continued to 1300ºC for 2 hours in air with a heating rate of 5 degrees per minute and cooling rate of 10 degrees per minute. The final product was Al_2O_3 solid lattices with approximately isotropic linear shrinkage of 32% in all three dimensions and ligament shrinkage of 32%. This results in a final sintered material density of 85% (relative to fully-dense bulk ceramic) for the base material of which the truss is made up. Bulk mechanical properties of alumina were measured by compression loading of commercially-obtained 99.5% pure alumina (AD-995, CoorsTek, Golden, CO). The values of Young's modulus and yield strength from these measurements are $E_s = 180$ GPa and $\sigma_s = 1.6$ GPa.

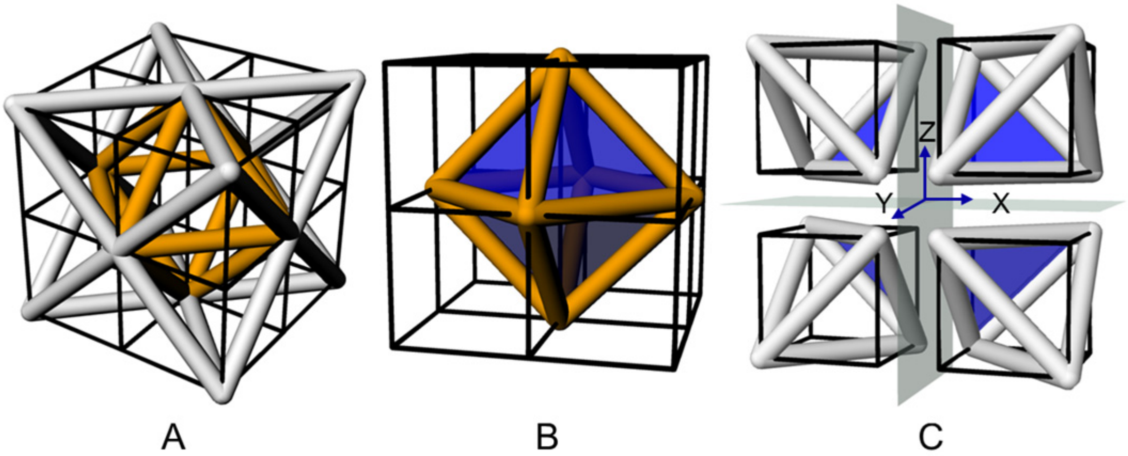

Fig. S1.

Cubic symmetry of the octet-truss unit cell. (A) Octet-truss unit cell with an octahedral core, and each surrounding quadrant containing one tetrahedral subunit. (B) The octahedral core of the unit cell with eight symmetry-equivalent faces, corresponding to the eight equivalent orientations in the (111) family. (C) Symmetry of the tetrahedral subunits, and the (111) family of symmetry-equivalent planes.

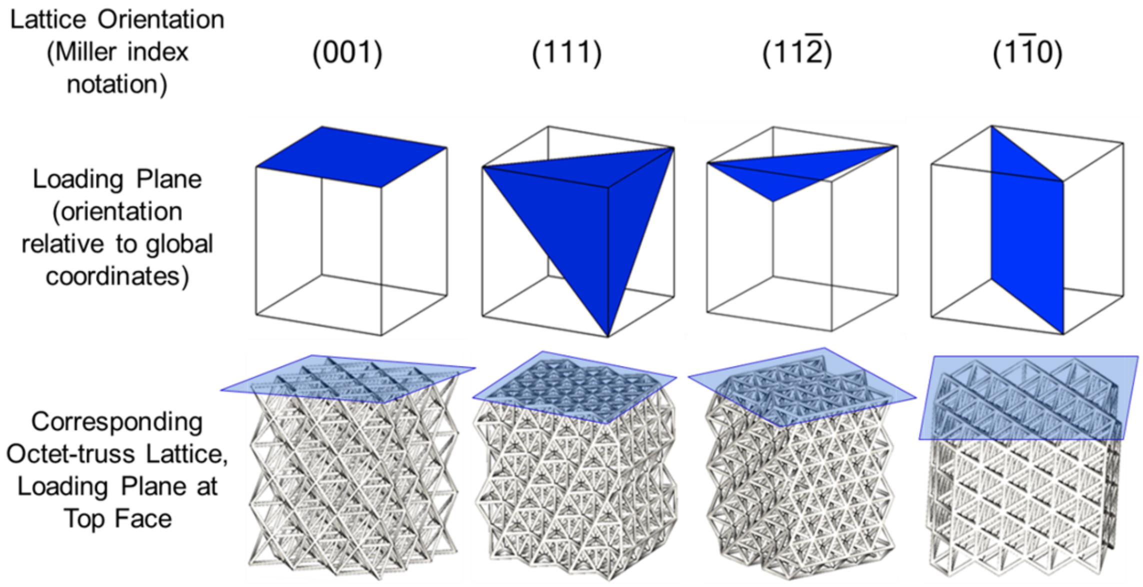

Fig. S2

Illustration of the different loading orientations of octet-truss lattices studied in this work. Lattice orientations are referred to by the Miller indices of the lattice plane to which loading is applied. A (111)-oriented lattice has a (111) plane at its top surface, to which uniaxial compressive loading is applied in the [111] direction.

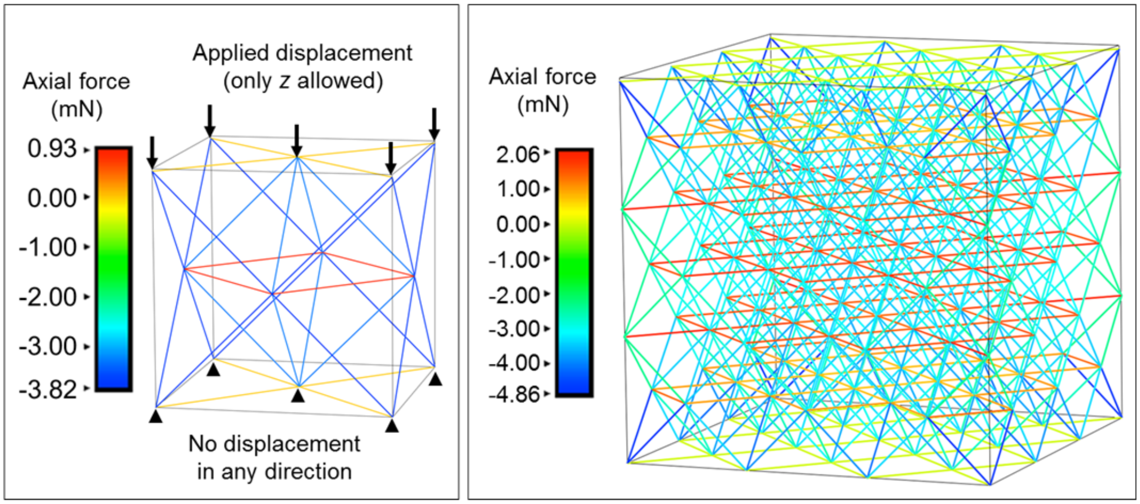

Fig. S3

Illustration of the NIKE3D FEM simulation used to study the directional stiffness dependence of the octet-truss lattice, indicating the boundary conditions for the simulations, and the calculated axial forces for each strut. A single unit cell is shown at left, and a 3x3x3 lattice at right.

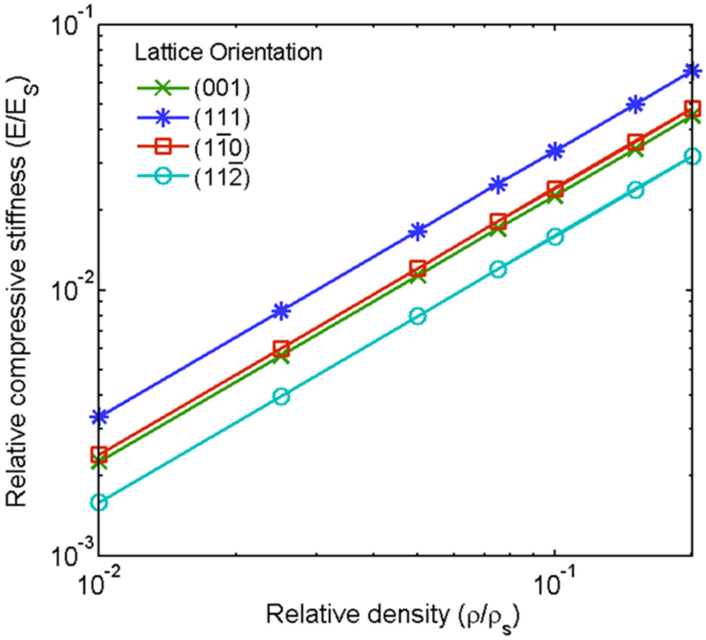

Fig. S4

The results of FEM investigation showing relative compressive stiffness as a function of relative density of octet-truss lattices in different loading orientations.

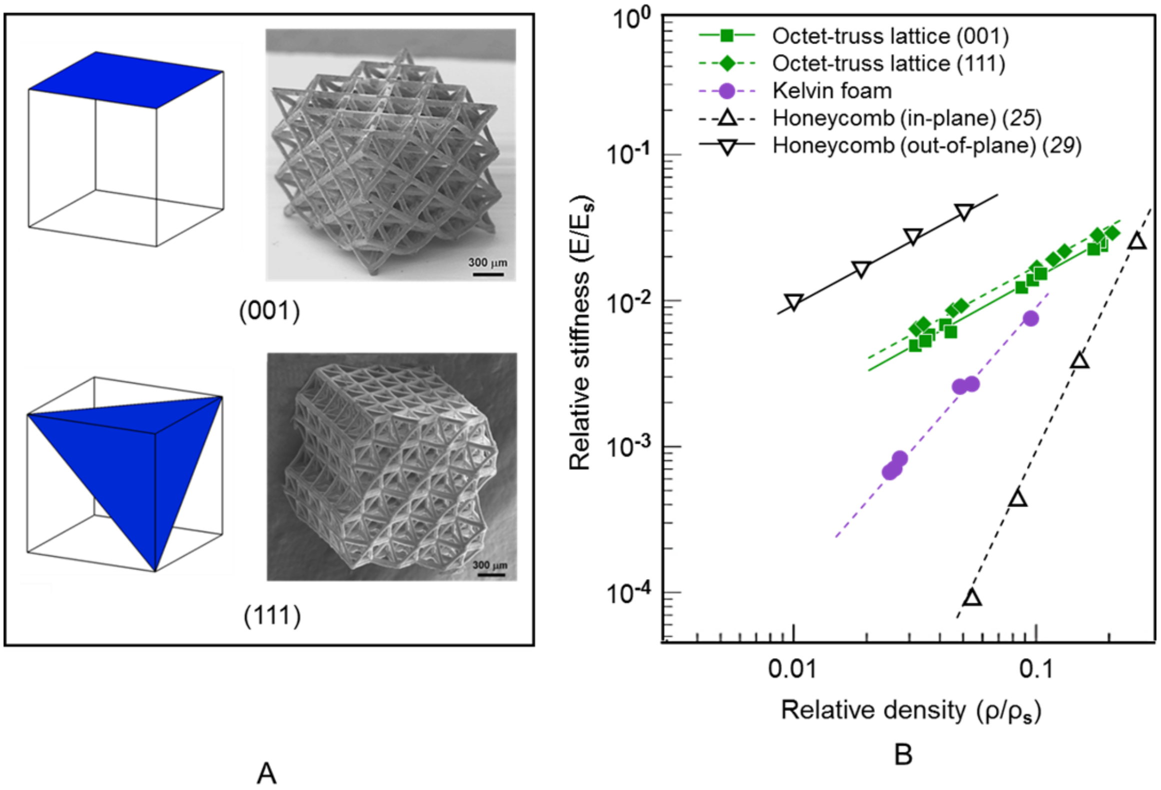

Fig. S5

(A) Two orientations of 1 mm x 1 mm x 1 mm octet-truss lattices fabricated by projection micro-stereolithography. (B) Relative compressive stiffness of octet-truss lattices in (001) and (111) orientations, shown as a function of relative density, in comparison with honeycomb structures loaded both in-plane and out-of-plane, as well as a bend-dominated open cell tetrakaidekahedral (Kelvin) foam, also fabricated by projection micro-stereolithography. The lines are linear fits to the measured data points.

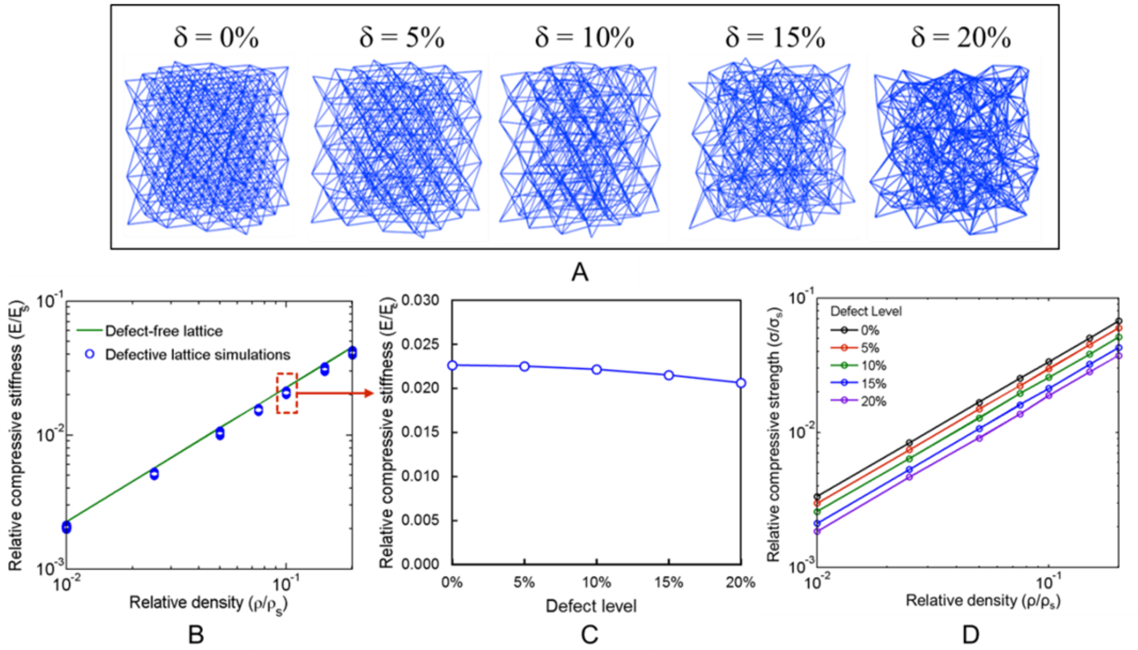

Fig. S6

Defect sensitivity study of octet-truss lattices. (A) The nodes of a (001)-oriented lattice are displaced by a prescribed Gaussian distribution with zero mean and a standard deviation of 5-20% of the strut length. (B) The straight line is the $E{\sim}\sigma$ relationship of an octet-truss lattice without defects. Each cluster of data points for a given relative density spans the range of geometric defects from 5% to 20%. (C) A typical detailed view of the relative stiffness as a function of defect level at one relative density (11%) indicated by the box and arrow in (B). (D) Relative yield strength vs. relative density of octet-truss lattices with varying levels of geometric defects.

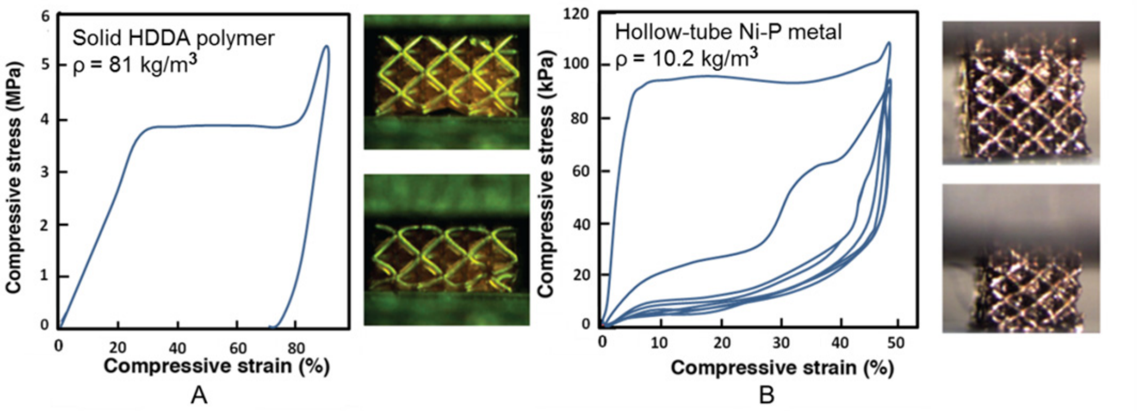

Fig. S7

Representative uniaxial compressive loading and unloading response of octet-truss microlattices. Strength σ_y is defined as the collapse stress of the lattice from uniaxial loading. Measurements are shown for (A) a solid HDDA polymer lattice ($\sigma_y = 3.8$ MPa) and (B) a Ni-P hollow-tube metallic lattice ($\sigma_y = 90$ KPa).

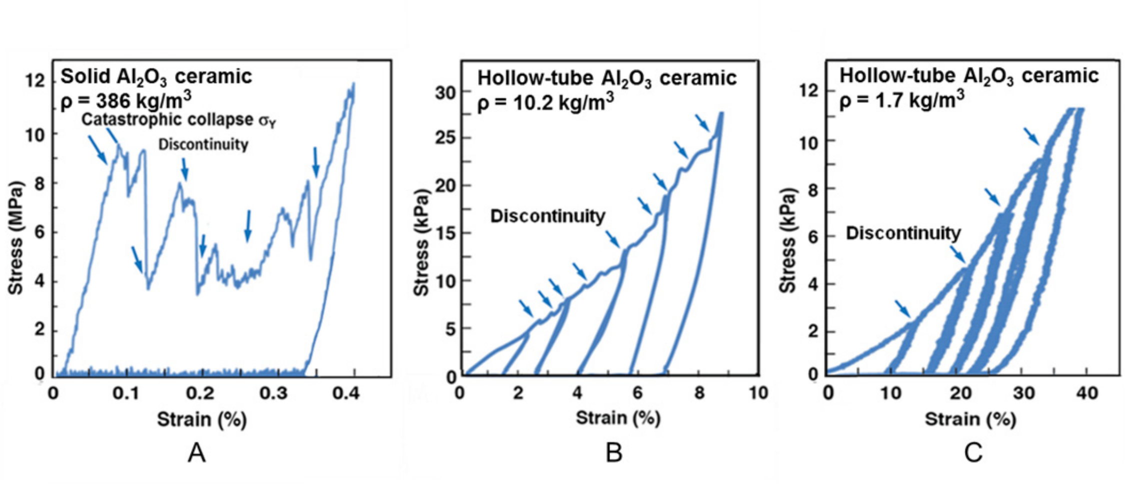

Fig. S8

Stress-strain curves obtained from cyclic uniaxial compression of Al_2O_3 octet-truss microlattices. (A) Catastrophic collapse was observed at first loading in the solid Al_2O_3 lattice with a density of 386 kg/m^3. (B) and (C) For hollow-tube Al_2O_3 lattices with mass densities of 10.2 kg/m^3 and 1.7 kg/m^3 , respectively, compression was performed to progressively larger stress with complete unloading between each cycle. Discontinuities which are attributed to local collapses in are indicated by arrows in the stress strain curves.

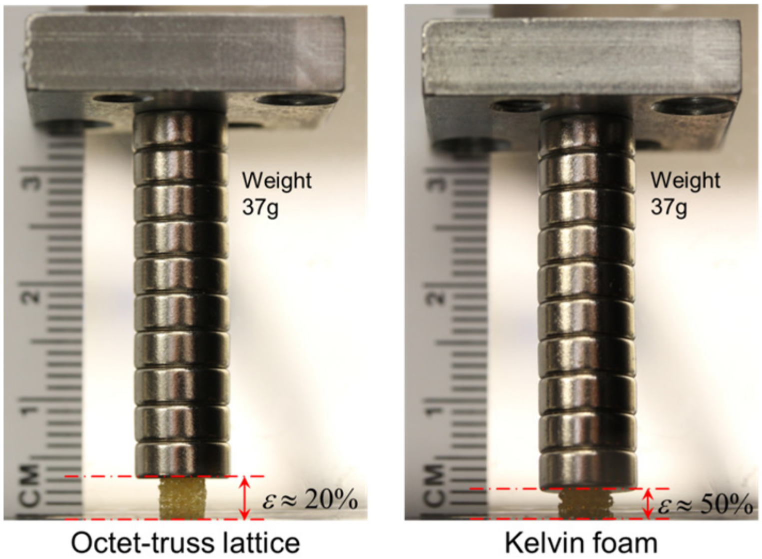

Fig. S9

A weight-bearing comparison between stretch- and bend-dominated lattices. 4x4x4 mm^3 solid polymeric microlattices, both fabricated from the same PEGDA material with a relative density of 5%, carrying at least 160,000 times their own weight. The octet-truss microlattice at left demonstrates markedly superior specific stiffness compared with the open-cell foam (Kelvin foam) at right.

Table S1.

Summary of geometric and material properties for selected microlattices fabricated in this work.

Lattice Material and Architecture	HDDA (solid) Octet-truss Lattice				Ni-P (hollow-tube) Octet-truss Lattice							HDDA (solid) Kelvin Foam			Al_2O_3 (hollow-tube) Octet-truss Lattice			
Overall Dimensions X,Y, Z (mm)	1.16 1.09 0.94	1.18 1.12 1.08	1.0 1.12 1.03	1.0 0.98 1.05	1.06 1.18 1.1	1.12 1.06 1.02	1.1 0.98 1.03	1.02 1.0 1.0	1.02 1.0 1.0	0.96 1.0 1.0	1.02 0.94 1.0	1.0 1.05 1.0	1.08 1.0 1.0	1.0 0.95 1.0	1.1 1.13 1.1	1.0 1.1 1.12	5.1 3.2 3	1.1 1.0 1.12
Mass (µg)	148	125	48	59	14	28	69.7	41.8	13	20.1	55.6	165	137	218	14.7	4.6	93	1.7
Density (kg/m^3)	125	96	41.6	57.3	10.2	23	62.8	41	10	21	58	158	127	228	10.8	3.1	1.9	1.4
Relative Density (%)	10.4	8.0	3	5	0.12	0.25	0.71	0.46	0.1	0.24	0.7	13	10.6	19	0.3	0.10	0.066	0.048
Wall Thickness (nm)	-	-	-	-	100	180	500	340	100	120	500	-	-	-	100	50	40	40
Stiffness (MPa)	7.59	5.8	2.7	3.9	11	22	70	47	9.8	23	55	3.4	3.1	10.1	44	8.2	3.9	3.6
Yield stress (MPa)	2.7	2.3	0.9	1.2	0.09	0.83	2.21	1.84	0.07	1.2	2.2	1.7	1.2	2.9	0.12	0.042	0.026	0.009

Movie S1

Uniaxial incremental cyclic compression of a 5% solid polymer (HDDA) bend-dominated lattice (played at 4x speed). Compression was actuated using a precision air-bearing three-axis positioning system (Aerotek, Inc., Pittsburgh, PA). In the test configuration, the bottom surface remained fixed while the top surface was displaced in the vertical direction. Each successive compression cycle increases the lattice deformation by approximately 10% strain.

Movie S2

Uniaxial incremental cyclic compression of a 9.8% solid polymer (HDDA) stretch-dominated lattice (played at 4x speed). The equipment and test configuration are the same as Movie S1. Each successive compression cycle increases the lattice deformation by approximately 15% strain.

Movie S3

Uniaxial cyclic compression of a stretch-dominated ultralight hollow-tube Ni-P lattice (ρ=11.8 kg/m^3) with increases in lattice strain by approximately 10 μm at each subsequent loading cycle. The equipment and test configuration are the same as Movie S1.